ARCHIVIO ISTITUZIONALE
DELLA RICERCA

Alma Mater Studiorum Università di Bologna
Archivio istituzionale della ricerca

Metal abundances in the MACER simulations of the hot interstellar medium

This is the final peer-reviewed author's accepted manuscript (postprint) of the following publication:

Published Version:
Pellegrini S., G.Z. (2020). Metal abundances in the MACER simulations of the hot interstellar medium. ASTRONOMISCHE NACHRICHTEN, 341, 184-190 [10.1002/asna.202023776].

Availability:
This version is available at: https://hdl.handle.net/11585/801062 since: 2022-11-10

Published:

DOI: http://doi.org/10.1002/asna.202023776

Terms of use:

Some rights reserved. The terms and conditions for the reuse of this version of the manuscript are specified in the publishing policy. For all terms of use and more information see the publisher's website.

This item was downloaded from IRIS Università di Bologna (https://cris.unibo.it/).
When citing, please refer to the published version.

(Article begins on next page)

11 October 2026

This is the final peer-reviewed accepted manuscript of:

Pellegrini, S., Gan, Z., Ostriker, J. P., & Ciotti, L. (2020). Metal abundances in the MACER simulations of the hot interstellar medium. *Astronomische Nachrichten*, *341*(2), 184–190.

The final published version is available online at:
https://doi.org/10.1002/asna.202023776

Rights / License:

The terms and conditions for the reuse of this version of the manuscript are specified in the publishing policy. For all terms of use and more information see the publisher's website.

.

This item was downloaded from IRIS Università di Bologna (https://cris.unibo.it/)

When citing, please refer to the published version.

Received 8 September 2019; | Revised XXX; | Accepted XXX

DOI: xxx/xxxx

ORIGINAL ARTICLE

Metal abundances in the MACER simulations of the hot interstellar medium

Silvia Pellegrini*[1] | Zhaoming Gan[2,3] | Jeremiah P. Ostriker[3] | Luca Ciotti[1]

[1]Department of Physics and Astronomy, University of Bologna, via Gobetti 93/2, 40129 Bologna, Italy
[2]Shanghai Astronomical Observatory, Chinese Academy of Sciences, 80 Nandan Road, Shanghai, People's Republic of China
[3]Department of Astronomy, Columbia University, 550 W, 120th Street, New York, NY 10027, USA

Correspondence
*S. Pellegrini, Dept. of Physics and Astronomy, University of Bologna, via Gobetti 93/2, I-40129 Bologna. Email: silvia.pellegrini@unibo.it

arXiv:1912.05857v1 [astro-ph.GA] 12 Dec 2019

A hot plasma is the dominant phase of the interstellar medium of early-type galaxies. Its origin can reside in stellar mass losses, residual gas from the formation epoch, and accretion from outside of the galaxies. Its evolution is linked to the dynamical structure of the host galaxy, to the supernova and AGN feedback, and to (late-epoch) star formation, in a way that has yet to be fully undestood. Important clues about the origin and evolution of the hot gas come from the abundances of heavy metals, that have been studied with increasing detail with XMM-Newton and Chandra. We present recent high resolution hydrodynamical simulations of the hot gas evolution that include the above processes, and where several chemical species, originating in AGB stars and supernovae of type Ia and II, have also been considered. The high resolution, of few parsecs in the central galactic region, allows us to track the metal enrichment, transportation and dilution throughout the galaxy. The comparison of model results with observed abundances reveals a good agreement for the region enriched by the AGN wind, but also discrepancies for the diffuse hot gas; the latter indicate the need for a revision of standard assumptions, and/or the importance of neglected effects as those due to the dust, and/or residual uncertainties in deriving abundances from the X-ray spectra.

KEYWORDS:
galaxies: active – galaxies: ISM – ISM: abundances – ISM: evolution – X-rays: ISM

1 | INTRODUCTION

A hot plasma dominates the ISM of early-type galaxies, as discovered with *Einstein* X-ray observations, and investigated thoroughly until recently with *Chandra* and *XMM-Newton* (Fabbiano, 2012). The X-ray emission of this hot phase correlates with the main galaxy properties, as the optical luminosity, and the stellar and total galaxy mass, although with a significant scatter (Forbes et al., 2017; Goulding et al., 2016). The observed X-ray properties have led to a picture where the origin of the hot ISM is in the old, ageing stellar population, and perhaps also in circumgalactic infall (Pellegrini, Ciotti, Negri, & Ostriker, 2018; Werner, McNamara, Churazov, & Scannapieco, 2019); its evolution is the result of the main galactic properties, as the depth and shape of the potential well, and the stellar kinematics, and of important phenomena, such as heating from supernovae and AGN feedback, and late-epoch star formation [Ciotti, Pellegrini, Negri, & Ostriker (2017); Gan, Ciotti, Ostriker, & Yuan (2019), hereafter G19a; Negri, Posacki, Pellegrini, & Ciotti (2014)]. While the respective roles of these processes are not fully understood yet, it is expected that they contribute to the enrichment of the gas in metals, and, that, during its evolution, they are able to circulate the metals within and outside the galaxies. Thus, metals provide important diagnostic tests for the ISM origin and the mentioned processes regulating its evolution. In the hydrodynamical MACER code for the evolution of the ISM of massive

elliptical galaxies (G19a), element tracers have recently been added in order to track the metal enrichment, transportation, and dilution throughout the galaxy, and outside [Gan, Choi, Ostriker, Ciotti, & Pellegrini (2019), hereafter G19b]. In the following we briefly describe the MACER modeling (Sect. 2), with particular emphasis on the sources of mass and metals for the hot ISM (Sect. 2.1); we then present the results of the simulations for the metals only (Sect. 3), and the conclusions (Sect. 4) that include a comparison with observations.

2 | MODELING THE ISM EVOLUTION

The physical modeling of the ISM evolution has been implemented in grid-type hydrodynamical simulations, performed with the Athena++ code (see G19a,b). The main advantages of these simulations are the accurate treatment of the sources of mass and heating, the latter from SNe and the AGN, and the high resolution, that reaches 2.5 pc at the center, so that the fiducial Bondi radius for accretion onto the central massive black hole (hereafter MBH) is resolved. The ISM evolution is followed from an age of 2 Gyr (after the main galaxy formation phase) until the present epoch, for a time interval of 11 Gyr.

The code solves the time-dependent Eulerian hydrodynamical equations with sources and sinks of mass, energy, and momentum. Sources of mass are provided by three channels: 1) the original, ageing stellar population, 2) the new stars [cold, dense gas is allowed to form stars, following both a Jeans criterion and Toomre instability criterion; see G19a for more details], and 3) accretion from the circumgalactic medium (hereafter CGM). No mass loading of cold gas into the hot phase is considered. These mass sources in turn provide metals (Sect. 2.1). Sources of heating for the gas come from SNe explosions (of types SNIa and SNII, the latter only from the new stars, with a thermalization efficiency of 0.85), from the thermalization of the stellar motions, and from accretion onto the MBH. Accretion produces a nuclear luminosity, with an efficiency scaling with the mass accretion rate, with the consequent radiative feedback; it also produces mechanical feedback via AGN winds, with maximum velocities of 10^4 km s^{-1}, and a mechanical efficiency again scaling with the mass accretion rate, as observed for nuclear outflows (Arav, Borguet, Chamberlain, Edmonds, & Danforth, 2013; Carniani et al., 2015; Tombesi et al., 2015). More details are given in G19a.

An important feature of the modeling is the implementation of streaming velocity for the stars; this imparts net angular momentum to their mass losses, so that the gas, when infalling in a cooling flow, settles in a rotationally supported disk-like structure; gas then cools in the disk, where it becomes gravitationally unstable, according to the Toomre Instability, and new stars form. Angular momentum transfer and star formation are then allowed at the same time, with the consequent near coincidence of star formation and AGN activity.

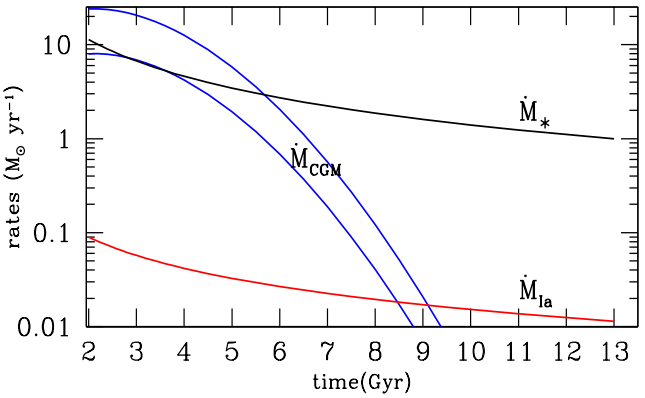

FIGURE 1 The mass input rates to the ISM from the old stellar population (AGB winds, in black, $\dot{M}_\star$; and SNIa's ejecta, in red, $\dot{M}_{\rm Ia}$), and from the cosmological CGM infall (in blue, $\dot{M}_{\rm CGM}$, for the two normalizations of $\rm CGM_{20}$ and $\rm CGM_7$ models). The $\dot{M}_\star$ and $\dot{M}_{\rm Ia}$ rates refer to the galaxy with $M_\star = 3.3\times10^{11}\rm M_\odot$ of Sect. 3. See Sect. 2.1 for more details.

2.1 | Sources of mass and metals

Mass sources to the ISM are due to stars and the CGM. The initial, old stellar population (hereafter SSP) injects mass via AGB winds, at a mass rate $\dot{M}_\star$, and, to a much lesser extent, via SNIa's ejecta at a mass rate $\dot{M}_{\rm Ia}$. As described in Pellegrini (2012), the rates of these processes, after an age $t_{\rm age} = 2$ Gyr for the SSP, are:

$$\dot{M}_\star = 10^{-12} A \frac{M_\star}{M_\odot}\left(\frac{t_{\rm age}}{12\rm Gyr}\right)^{-1.3} \qquad M_\odot \rm yr^{-1} \qquad (1)$$

where $A = 3.3$ for the Kroupa IMF, and $M_\star$ is the SSP mass at $t_{\rm age} = 12$ Gyr, and:

$$\dot{M}_{\rm Ia} = 0.216\times10^{-12}\frac{L_{\rm B}}{L_{B\odot}}\left(\frac{t_{\rm age}}{12\rm Gyr}\right)^{-1.1} \qquad M_\odot \rm yr^{-1} \qquad (2)$$

where $L_{\rm B}$ is the present-epoch B-band luminosity of the SSP; and $1.35M_\odot$ for the mass ejected in one SNIa event, and a Hubble constant of 70 km s^{-1} Mpc^{-1}, have been assumed.

New stars form in the cold gas disk with a top-heavy IMF of index equal to -1.65, based on observations (e.g., the central stellar disks in the Milky Way and M31), and theoretical expectations (Bartko et al., 2010; Jiang & Goodman, 2011; Lu et al., 2013). The chosen IMF has $\sim 60\%$ of the new star mass in massive stars which turn into SNII; for the new stars, only SNII provide a source of mass and metals to the ISM (G19b).

Infall of the CGM onto the galaxy also provides mass to the ISM, at a rate ($\dot{M}_{\rm CGM}$) estimated from cosmological zoom-in

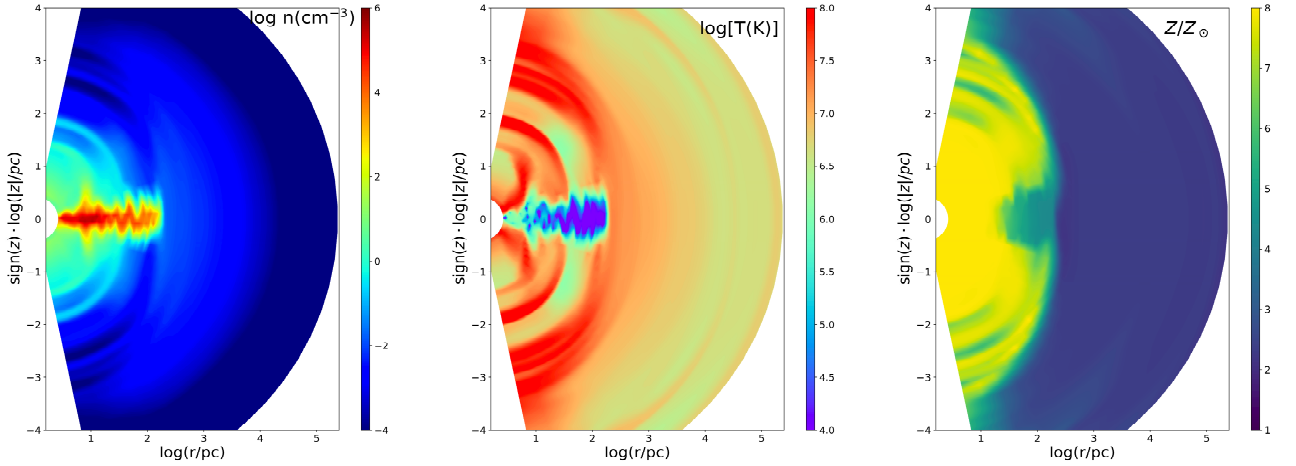

FIGURE 2 Meridional sections of the ISM density (left), temperature (middle), and abundance Z of all metals (right), for the ISM in the galaxy model described in Sect. 3, during a nuclear outburst. The cold disk is evident, as the increase in Z above and below it, produced by the AGN wind.

simulations, based on the evolution of the accretion rate for 30 massive ellipticals [Brennan et al. (2018), G19a]. The rate declines sharply as expected in a Λ−CDM universe. Figure 1 shows a comparison of the mass input rates from the SSP and the CGM infall, during the time span of the simulations. We adopt two normalizations for the CGM infall rate, within the range shown by cosmological simulations; the corresponding total accreted mass during the time interval in Figure 1 is 1/20 (for CGM_{20} models) and 1/7 (for CGM_7 models) of $M_\star$. For comparison, the total injected mass from the SSP amounts to $M_\star/10$, during the same time.

The three sources of mass considered above (old and new stars, and the CGM) also provide metals to the ISM. In the code the chemical evolution of the ISM due to the injection, dilution, and transportation of metals is followed introducing 12 tracers X_i (i=1, 2, ... 12), where X_i is the mass of the i-th element per unit volume. The elements considered are H, He, C, N, O, Ne, Mg, Si, S, Ca, Fe, and Ni. Thus, 12 additional continuity equations are solved, assuming the chemical species comove after they are injected into the ISM:

$$\frac{\partial X_i}{\partial t} + \nabla \cdot (X_i \boldsymbol{v}) + \nabla \cdot \dot{\mathbf{m}}_{Q,i} = \dot{X}_{i,\star} + \dot{X}_{i,\mathrm{Ia}} + \dot{X}_{i,\mathrm{II}} - \dot{X}_{i,\mathrm{SF}}, \quad (3)$$

where $\boldsymbol{v}$ is the gas velocity; the different metal-enriching sources from AGB winds ($\dot{X}_{i,\star}$), SNIa's ($\dot{X}_{i,\mathrm{Ia}}$), and SNII's ($\dot{X}_{i,\mathrm{II}}$) are evidenced; star formation $\dot{X}_{i,\mathrm{SF}} = (X_i/\rho) \cdot \dot{\rho}_{\mathrm{SF}}$, where ρ is the gas density and $\dot{\rho}_{\mathrm{SF}}$ is the gas sink due to star formation, is treated as a sink of local metals; and $\dot{\mathbf{m}}_{Q,i} = (X_i/\rho) \cdot \dot{\mathbf{m}}_Q$, where $\dot{\mathbf{m}}_Q$ is the momentum density for the gas that becomes Toomre-unstable (see G19b for more details).

The simulations start at an age of 2 Gyr, therefore the SSP contributes metals only via AGB winds and SNIa's ejecta. The weakly time-dependent metal input from AGB winds was calculated with âĂIJCELib,âĂİ an open-source software library for chemical evolution (Saitoh, 2017). The abundance of the SSP is $Z_\star$=1.5$Z_\odot$ [where $Z_\odot$ = 0.0134, Asplund, Grevesse, Sauval, & Scott (2009)], as appropriate for a massive elliptical as the modeled one (Thomas, Maraston, Schawinski, Sarzi, & Silk, 2010). The nucleosynthetic yields of SNIa's are those of the N100 model of Seitenzahl et al. (2013), dominated by Fe and Si. The SNII yields are those of Nomoto, Kobayashi, & Tominaga (2013), and average values are calculated for the progenitor's masses born with the adopted IMF of the new stars (see G19b for more details).

The CGM infall provides low-metallicity gas with Z_{CGM} = 0.002 (i.e., Z_{CGM}=0.15$Z_\odot$). This gas accretes through the galaxy outskirts, and produces a dilution of the abundance of the ISM of internal origin as it falls into the galaxy and mixes with the ISM. It does not appear explicitly in equation 3, since the CGM infall is implemented as an outer boundary condition.

3 | RESULTS

We present the resulting chemical evolution of the ISM for an E2 elliptical galaxy, of stellar mass at the present epoch of $M_\star = 3.3 \times 10^{11} \mathrm{M}_\odot$, effective radius R_e = 7 kpc, and central stellar velocity dispersion of 280 kms^{-1}. A central MBH and a spherical dark matter halo are also added, and the ordered rotational velocity of the stellar component is given by the Satoh decomposition, with exponentially declining rotation parameter k (see G19b). The presence of streaming velocity results for the ISM into the formation of a central cold disk, where

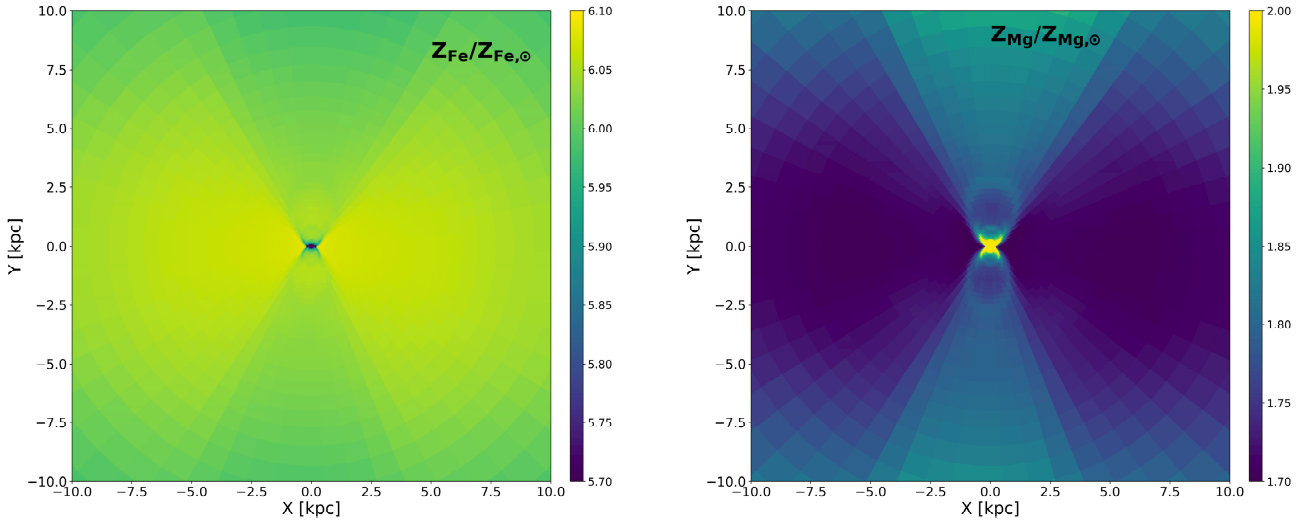

FIGURE 3 Map of the emission weighted and projected abundance of Fe (left) and Mg (right), for the ISM in the galaxy model described in Sect. 3; the snapshot is taken during a nuclear outburst, at the same time of Figure 2 ; note the linear scale instead of the logarithmic one used in Figure 2 .

star formation takes place; the latter becomes then an important metal-enriching source, mostly by SNe II. In fact, the ISM evolution undergoes recurrent cycles during which the gas accumulates in the disk, until when the Toomre instability sets in, allowing for star formation and mass inflow from the disk towards the MBH. Thus, with a short delay, star formation is followed by accretion of disk material onto the MBH, whose feedback action via biconical BAL (broad absorption line) winds causes the ejection of recently metal-enriched gas from the disk (Figure 2). The abundance of the BAL winds is evaluated by tracking the chemical composition of the mass accreted via the inner boundary; the metals passing through the center are present in the BAL winds and injected back to the galaxy from its nucleus. Freshly produced metals are spread out to large distances (of $\simeq$ 1 kpc and more); the abundance of the high velocity, outward-moving gas, can be many times solar. Note that these high abundances are fundamental for the gas surrounding the MBH to be multiphase, and include a stable gas phase representing the broad line region (BLR) clouds (Chakravorty, Kembhavi, Elvis, & Ferland, 2009).

Figure 2 shows the density and temperature of the ISM during an outburst. The cold disk, extending for $r \simeq 150$ pc, is clearly visible, as is the biconical wind structure in the temperature map. Note that the size of the cold disk strongly depends on the galaxy rotation profile. In the right panel the total abundance Z is shown (the logarithmic scale on the axes emphasizes the central region). SNII products, transported by the winds, contaminate the region above and below the disk; they reveal many subsequent ejection episodes closely spaced in time, that took place during the nuclear outburst. As an example, in the outflowing region affected by the BAL wind with a radial velocity $v_r \geq 10^3$ km s^{-1}, the mass-weighted average abundance is $4Z_\odot$ (with a weighting towards products from SNII).

Figure 3 shows the emission weighted and projected maps for the abundance of Fe and Mg, at the same time of Figure 2 during the outburst. Interestingly, these two metal species show an opposite behavior. In fact, star formation increases the overall Z of the ISM, but in the SNII ejecta the Fe is less abundant than in the mass lost by the old SSP. This causes Fe to be more abundant over the main galaxy body, and less abundant in the region affected by recent star formation (the central disk and the biconical region affected by the spreading of metals due to the BAL winds). The symmetric behavior is shown by Mg, that is more abundant in the regions affected by SNII ejecta. Thus, SNII-products as Mg are a tracer of the distances reached by the ISM driven by the AGN winds. Note that the biconical region in Figure 2 comes from the subsequent action of many outbursts during the galaxy's lifetime, and that each outburst produces an abundance pattern rich in substructure, that cannot be shown here due to the limited space.

Figure 4 shows the emission-weighted, projected and circularized abundance profile, Z(R), for the ISM when the SSP age is 12 Gyr. Also shown is the abundance of the mass contributed by the SSP sources (AGB+SNIa's; hereafter "passive" abundance Z_{old}). Since the SSP is assumed to be homogeneous

across the galaxy, Z_{old} is position-independent; it depends instead on the SSP age, since the metal injection of AGB winds and of SNIa's follows different time-dependencies (Sect. 2.1). In Figure 4 the values of Z_{old} at two ages of the SSP (2 and 13 Gyr) are shown. One notices that 1) Z_{old} varies in a narrow range[1], from 2.1 to 2.3 $Z_\odot$, over the whole time-span, and 2) Z(R) of the ISM when the SSP is 12 Gyr old (black line) is close to Z_{old}(13 Gyr): Z(R) is just slighly above it, due to the enrichment contributed by new stars, and does not show pronounced radial trends. The black line in the figure refers to the CGM_{20} model, the same shown in Figures 2 and 3; the red line refers instead to its CGM_7 version, with a larger CGM infall (Sect. 2.1). The CGM_7 model shows a large radial gradient: its Z(R) is comparable to that of CGM_{20} in the central galactic region, but decreases outer of $R \sim 15$ kpc. The abundance of the ISM averaged *over the whole galaxy* is 2.4 $Z_\odot$ for the CGM_{20} model, dropping to $\sim 1.5 Z_\odot$ for the CGM_7 one.

Figure 5 shows the emission-weighted, projected and circularized Fe abundance profile, Fe(R), for the ISM when the SSP age is 12 Gyr, again with the "passive" Fe abundance (Fe_{old}) at 2 and 13 Gyr of age for the SSP, and the CGM_7 model included for comparison. The same trends of Figure 4 are apparent, with one difference: Fe(R) keeps below Fe_{old}(13 Gyr), even at the center. This is explained by the fact that Fe_{old} is time-increasing, and the SSP age for the plotted ISM is 12 Gyr; and by the large difference in the Fe-production between the SPP and the new stars (see the discussion above for Figure 3). Figure 5 also shows the observed Fe(R) for a giant elliptical galaxy: except for the innermost point, outer of R≈20 kpc the agreement with the modeled ISM is good.

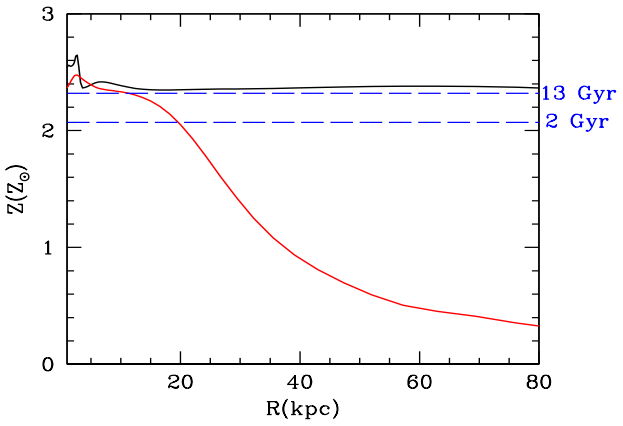

FIGURE 4 Emission-weighted, projected and circularized abundance of the ISM Z(R), for the CGM_{20} (in black) and CGM_7 (in red) models, for the galaxy described in Sect. 3, at an age of 12 Gyr. Also shown (in blue) are the abundances Z_{old} at two epochs, for the mass ejected by AGB winds+SNIa's (with $Z_\star = 1.5 Z_\odot$ for the SSP). The Z_{old} values are independent of the galaxy stellar mass, provided that the same IMF and $Z_\star$ apply (see Sect. 3 for more details).

4 | CONCLUSIONS

In the MACER code for the investigation of the evolution of the ISM of elliptical galaxies, at high spatial resolution and with AGN feedback, the metal enrichment, transportation, and dilution processes have recently been implemented (G19b). From these recent simulations for a massive elliptical, we have here emphasized the following results:

- the average Z of the hot ISM on the whole galactic scale is $\simeq 2.4 Z_\odot$; this value can go down to $\sim 1.5 Z_\odot$ when the CGM infall rate is closer to the largest estimates from cosmological simulations.
- for R < 15 kpc, Z(R) of the hot ISM is close to the 'passive' prediction (i.e., the abundance of AGB winds+SNIa's), independent of the cosmologically-motivated CGM infall rate. A small increase due to new star formation is present; this increase is disk-dependent, and thus related to the streaming velocity field of the host galaxy. Outer of $R \simeq 15$ kpc, Z(R) sharply decreases for the larger CGM infall rate.
- the Fe abundance profile Fe(R) follows the same trends shown by Z(R), with the difference of being *lowered* by the presence of new star formation. This feature is also shown in the abundance map of Fe, and is opposite to that shown in the Mg abundance map.
- during outbursts, the outflowing regions, driven by the BAL wind, can reach an abundance of Z≃ $4 Z_\odot$, and can transport metals (mostly SNII products made in the disk) out to large radii. This finding is in agreement with observations that Z of a quasar BLR in massive galaxies is 0.3 to 1.0 dex larger than Z of the host galaxies, and does not evolve with cosmic time, which implies that the metal enrichment is due to recent star formation, as in the simulations (Nagao, Marconi, & Maiolino, 2006; Xu et al., 2018).

While the results above are encouraging for the part concerning the role of AGN winds, the observed Z (and Fe) of the hot ISM reveal more problematic issues. Observed values are generally solar, or slighlty supersolar, except for a few cases (one is shown in Figure 5), as established even recently, with the improved quality of both *Chandra* and XMM-*Newton* observations and data analysis (Humphrey & Buote, 2006; Loewenstein & Davis, 2010; Mernier et al., 2017, 2018). The

[1]The "passive" values in Figure 4 refer to the Kroupa IMF, but they would change very little for the Salpeter IMF.

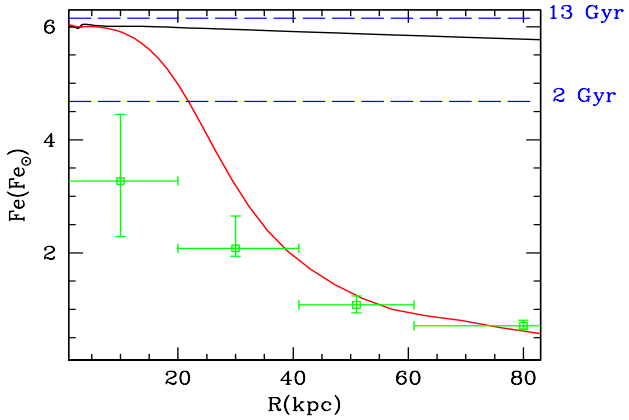

FIGURE 5 Emission-weighted, projected and circularized Fe abundance of the ISM, Fe(R), for the CGM_{20} (in black) and CGM_7 (in red) models, for the galaxy described in Sect. 3, at an age of 12 Gyr. Also shown (in blue) is Fe_{old} at two epochs, for the mass ejected by AGB winds+SNIa's (with $Fe_\star = 1.5 Fe_\odot$ for the SSP). Green squares show Fe(R) for NGC507, a dominant elliptical galaxy in a small group, from XMM-Newton observations (Kim & Fabbiano, 2004). See Sect. 3 for more details.

observed Z, and especially Fe, are lower than predicted by models, which represents an old problem, that has been alleviated in more recent investigations, but is clearly persisting. Contributing factors to it include residual uncertainties in the derived abundances, as for example due to the degeneracy of metallicity and emission measure, and the multi-temperature thermal structure of the ISM (de Plaa et al., 2017; Kim, 2012); dust depletion of metals (Lakhchaura, Mernier, & Werner, 2019; Panagoulia, Fabian, & Sanders, 2013); and incomplete mixing of SNIa's ejecta (Matsushita, Ohashi, & Makishima, 2000; Tang & Wang, 2010). Based on the present results, the CGM infall can also have an important effect. Another possibility is the mixing and stirring of metals between the inner and outer parts of the galaxies, as would be provided by a larger feedback wind efficiency, and/or infall of satellites. Finally, we emphasize that the depletion of metals onto dust has not been inserted in the models yet, and thus elemental abundances correspond to the total (dust plus gas phase) mass in that element. The depletion of refractory elements onto dust grains may be a large correction (Hensley, Ostriker, & Ciotti, 2014), and this subject is reserved to a future work.

REFERENCES

Arav, N., Borguet, B., Chamberlain, C., Edmonds, D., & Danforth, C. 2013, *MNRAS*, *436*, 3286.

Asplund, M., Grevesse, N., Sauval, A. J., & Scott, P. 2009, *ARAA*, *47*, 481.

Bartko, H., Martins, F., Trippe, S. et al. 2010, *ApJ*, *708*, 834.

Brennan, R., Choi, E., Somerville, R. S., Hirschmann, M., Naab, T., & Ostriker, J. P. 2018, *ApJ*, *860*, 14.

Carniani, S., Marconi, A., Maiolino, R. et al. 2015, *A&A*, *580*, 102.

Chakravorty, S., Kembhavi, A. K., Elvis, M., & Ferland, G. 2009, *MNRAS*, *393*, 83.

Ciotti, L., Pellegrini, S., Negri, A., & Ostriker, J. P. 2017, *ApJ*, *835*, 15.

de Plaa, J., Kaastra, J. S., Werner, N. et al. 2017, *A&A*, *607*, 98.

Fabbiano, G. 2012, in: Hot Interstellar Matter in Elliptical Galaxies, *Astrophysics and Space Science Library* (Vol. 378 p.1). Eds. D.-W. Kim, S. Pellegrini. Berlin: Springer.

Forbes, D. A., Alabi, A., Romanowsky, A. J., Kim, D.-W., P, B. J., & Fabbiano, G. 2017, *MNRAS*, *464*, 26.

Gan, Z., Choi, E., Ostriker, J. P., Ciotti, L., & Pellegrini, S. 2019, *ApJ*, *875*, 109 (G19b).

Gan, Z., Ciotti, L., Ostriker, J. P., & Yuan, F. 2019, *ApJ*, *872*, 167 (G19a).

Goulding, A. D., Greene, J. E., Ma, C.-P. et al. 2016, *ApJ*, *826*, 167.

Hensley, B. S., Ostriker, J. P., & Ciotti, L. 2014, *ApJ*, *789*, 78.

Humphrey, P. J., & Buote, D. A. 2006, *ApJ*, *639*, 136.

Jiang, Y.-F., & Goodman, J. 2011, *ApJ*, *730*, 45.

Kim, D.-W. 2012, in: Hot Interstellar Matter in Elliptical Galaxies, *Astrophysics and Space Science Library* (Vol. 378 p.121). Eds. D.-W. Kim, S. Pellegrini. Berlin: Springer.

Kim, D.-W., & Fabbiano, G. 2004, *ApJ*, *613*, 933.

Lakhchaura, K., Mernier, F., & Werner, N. 2019, *A&A*, *623*, 17.

Loewenstein, M., & Davis, D. S. 2010, *ApJ*, *716*, 384.

Lu, J. R., Do, T., Ghez, A. M., Morris, M. R., Yelda, S., & Matthews, K. 2013, *ApJ*, *764*, 155.

Matsushita, K., Ohashi, T., & Makishima, K. 2000, *PASJ*, *52*, 685.

Mernier, F., de Plaa, J., Kaastra, J. S. et al. 2017, *A&A*, *603*, A80.

Mernier, F., Werner, N., de Plaa, J. et al. 2018, *MNRAS*, *480*, L95.

Nagao, T., Marconi, A., & Maiolino, R. 2006, *A&A*, *447*, 157.

Negri, A., Posacki, S., Pellegrini, S., & Ciotti, L. 2014, *MNRAS*, *445*, 135.

Nomoto, K., Kobayashi, C., & Tominaga, N. 2013, *ARA&A*, *51*, 457.

Panagoulia, E. K., Fabian, A. C., & Sanders, J. S. 2013, *MNRAS*, *433*, 3290.

Pellegrini, S. 2012, in: Hot Interstellar Matter in Elliptical Galaxies, *Astrophysics and Space Science Library* (Vol. 378 p.21). Eds. D.-W. Kim, S. Pellegrini. Berlin: Springer.

Pellegrini, S., Ciotti, L., Negri, A., & Ostriker, J. P. 2018, *ApJ*, *856*, 115.

Saitoh, T. R. 2017, *AJ*, *153*, 85.

Seitenzahl, I. R., Ciaraldi-Schoolmann, F., Roepke, F. K. et al. 2013, *MNRAS*, *429*, 1156.

Tang, S., & Wang, Q. D. 2010, *MNRAS*, *408*, 1011.

Thomas, D., Maraston, C., Schawinski, K., Sarzi, M., & Silk, J. 2010, *MNRAS*, *404*, 1775.

Tombesi, F., Melendez, M., Veilleux, S., Reeves, J. N., Gonzalez-Alfonso, E., & Reynolds, C. S. 2015, *Nature*, *519*, 436.

Werner, N., McNamara, B. R., Churazov, E., & Scannapieco, E. 2019, *SSRv*, *215*, 5.

Xu, F., Bian, F., Shen, Y., Zuo, W., Fan, X., & Zhu, Z. 2018, *MNRAS*, *480*, 345.

How cite this article: Pellegrini S., Z. Gan, J.P. Ostriker, and L. Ciotti (2019), Metal abundances in the MACER simulations of the hot interstellar medium, *Astron. Nachr.*, *2019;00:1–6*.

How cite this article: Pellegrini S., Z. Gan, J.P. Ostriker, and L. Ciotti (2019), Metal abundances in the MACER simulations of the hot interstellar medium, *Astron. Nachr.*, *2019;00:1–6*.